On Microstructure Development During Laser Melting and Resolidification: an Experimentally Validated Simulation Study

Alexander F Chadwick, Juan Guillermo Santos Macías, Arash Samaei, Gregory Wagner, Manas V Upadhyay, Peter W Voorhees

To cite this version:

Alexander F Chadwick, Juan Guillermo Santos Macías, Arash Samaei, Gregory Wagner, Manas V Upadhyay, et al.. On Microstructure Development During Laser Melting and Resolidification: an Experimentally Validated Simulation Study. 2024. hal-04738571

HAL Id: hal-04738571
https://polytechnique.hal.science/hal-04738571v1

Preprint submitted on 15 Oct 2024

On Microstructure Development During Laser Melting and Resolidification: an Experimentally Validated Simulation Study

Alexander F. Chadwick[a,1,*], Juan Guillermo Santos Macías[b,2], Arash Samaei[c], Gregory Wagner[c], Manas V. Upadhyay[b,*], Peter W. Voorhees[a]

[a]*Department of Materials Science and Engineering, Northwestern University, 2220 Campus Drive, Evanston, IL 60208 USA*
[b]*Laboratoire de Mécanique des Solides (LMS), CNRS UMR 7649, École Polytechnique, Institut Polytechnique de Paris, 91128 Palaiseau, France*
[c]*Department of Mechanical Engineering, Northwestern University, 2145 Sheridan Road, Evanston, IL 60208 USA*

Abstract

Integrating experiment and simulation provides invaluable insights into the critical parameters that determine the microstructure of alloys produced by additive manufacturing. Here, the grain structure formation due to solidification during single pass laser scans (mimicking bead-on-plate single tracks) on a 316L stainless steel is studied *in situ* inside a scanning electron microscope that is directly integrated with a continuous-wave laser. The grain size distribution before melting is used as an initial condition in a coupled phase-field/thermal multiphysics modeling framework. The predicted resolidified microstructures are found to agree favorably with those observed experimentally for multiple laser powers and scan velocities, indicating the validity of the overall model. Grain morphology is analyzed quantitatively, and the top surfaces are compared between the experiments and simulations. Analysis of the three-dimensional grain shapes predicted by the simulations shows that the length of the major axis of the resolidified grains is sensitive to laser power and scan speeds, while the length of the minor axis is not. Furthermore, the preferential alignment of the major axes of the grains depends on the melt pool geometry.

Keywords: Additive manufacturing, Multiphysics modeling, Solidification, Laser polishing, Phase-field method, Computational fluid dynamics, Scanning electron microscopy

1. Introduction

There has been significant interest from the community to understand the melting and subsequent resolidification of metal alloys undergoing additive manufacturing (AM). However, there remains an ongoing motivation to develop computational models that can predict the as-solidified microstructures and grain morphologies [1, 2]. In processes such as laser powder bed fusion (LPBF), hundreds or thousands of grains may be exposed to the solid-liquid interface, creating a uniquely competitive set of resolidification kinetics as the orientations along the interface continuously change. The richness of this process and its interplay with heat and mass transport introduces significant complexity to the obtained microstructures and their evolution, which has concurrently motivated the need for model validation against benchmark datasets [3–7]. To date, models that adopt cellular automata (CA) and kinetic Monte Carlo (KMC) approaches have attracted the most interest at predicting the grain structure that forms within individual laser tracks or across the entire build [8–29]. These methods adopt a rules-based or stochastic description of a predetermined “growth law” to update the voxel representation of a microstructure from one time step to the next. Both CA and KMC can be implemented in computationally efficient manners, which allows them to consider rather large simulation volumes. This has allowed models to obtain quantitative agreement of key features such as

---

[*] Corresponding Authors

Email addresses: `alexander.f.chadwick.civ@us.navy.mil` (Alexander F. Chadwick), `manas.upadhyay@polytechnique.edu` (Manas V. Upadhyay)

[1] Present address: U.S. Naval Research Laboratory, 4555 Overlook Avenue SW, Washington, DC 20375 USA.

[2] Present address: Instituto madrileño de estudios avanzados materiales (IMDEA materiales), Calle Eric Kandel 2, 28906 Getafe, Spain.

crystallographic texture for representative volumes of a full build [9, 23, 26, 27]. However, the rules-based nature of these methods is not always readily generalized. For example, the usual Decentered Octahedra CA formulation assumes a single-phase material that only grows along $\langle 100 \rangle$ crystallographic directions [30].

Another possible modeling technique is the phase-field method (PFM[3]), which has been applied to understand microstructure and composition development in AM processes [11, 31–43]. PFMs are a powerful general tool that can be formulated to capture a wide variety of materials physics. This generality often carries considerable computational cost, although there is interest in either developing reduced-order models or parameterizing the CA model to accurately reproduce the microstructure produced by a PFM [11, 35]. The computational expense has also presented a barrier in validating PFMs of the AM process against experiments. Pinomaa *et al.* performed a convergence study of a two-dimensional (2D) PFM against thin-film experiments of rapid solidification in Al-Cu alloys and obtained quantitative agreement in the interfacial velocity as well as similar microstructures and solute concentration distributions [31]. Similarly, Karayagiz *et al.* observed agreement in the primary dendrite arm spacing and cellular-to-planar solidification transition in a 2D PFM of Ni-Nb alloys [32]. Although their approaches neglect the latent heat of solidification, the studies of both Liu *et al.* [42] and Yang *et al.* [33] obtained agreement with experiment when predicting certain aspects of the grain morphologies in Ti-6Al-4V and 316L stainless steel, respectively. Beyond these examples, there are also several works that have performed verification studies against analytical models to demonstrate model correctness [34, 35, 39, 43]. However, validation of three-dimensional (3D) PFMs against experiments at the scale of a melt track does not appear to have been investigated.

Recently, Santos Macías *et al.* coupled a continuous-wave laser and a scanning electron microscope (CW Laser-SEM) [44]. The purpose of this device is to perform laser scanning in a controlled environment (e.g., secondary vacuum or stationary inert gas to prevent oxidation) that can be reproduced in an AM machine, thus providing a platform for physical simulation. The added advantage of this device is that microstructure characterization before and after laser scanning is possible without the need to re-polish samples between measurements. Consequently, laser scanning inside the CW Laser-SEM offers more control over initial and boundary conditions of the problem and provides microstructural input as well as post-laser scan data for a one-to-one comparison with simulations. Recently, Mohanan *et al.* [45] used microstructural input from one of the studies conducted by Santos Macías et al. [44] to drive thermomechanical polycrystalline simulations and studied the evolution of intergranular residual stresses and plastic strains due to laser scanning. A one-to-one comparison of the predicted and experimentally derived dislocation density (Nye's) tensor was performed, and it demonstrated a good match at the statistical level [45]. Importantly, this comparative study highlighted the significant potential of CW Laser-SEM to test and validate the predictive capabilities of microstructure models.

Here, we present a study of a modeling framework to predict the as-solidified microstructure after laser melting and resolidification in the CW Laser-SEM. This framework couples an analytically verified PFM [34, 36, 37] with a separate thermal multiphysics model [46]. We validate the modeling framework by comparing morphological features from the model against CW Laser-SEM experimental data and examining how microstructures vary as a function of the input power and scan velocity. With the model, we also examine 3D morphological data of the predicted microstructures and the orientations of the principal axes of grains with respect to the scan direction.

2. Experimental Methods

The base material used in the experiment was hot rolled, annealed and pickled 316L stainless steel (see Table 1 for composition) with an average grain size of 11.6 µm when the twins are not merged with their parent grains. A $15 \times 10 \times 10$ mm^3 piece was ground using SiC grinding paper, then polished with diamond paste down to 1 µm particle size. The laser parameters employed are listed in Table 2. All scans were performed under vacuum with a constant spot size of 60 µm. For each set of laser parameters, a line scan was performed on the polished surface. The tracks were parallel and spaced 350 µm apart to avoid interference. EBSD was performed with a 0.5 µm step size on the same sample surface before and after lasering.

---

[3] Throughout this work, PFM refers to phase-field method or phase-field model as appropriate.

Element	Fe	Cr	Ni	Mo	Mn	Si	Co	Cu	N	P	C	S
wt.%	69.072	16.52	10.08	2.08	1.31	0.5	0.31	0.036	0.033	0.033	0.024	0.002

Table 1: Chemical composition (wt.%) of the base 316L material.

Track	Power (W)	Speed (mm/s)
1	66	150
2	45	150
3	66	250
4	45	250
5	24	150
6	66	500
7	24	250
8	45	500
9	24	500

Table 2: Lasering parameters employed in the present study.

To validate the model that is developed in this work, laser scanning experiments were performed on the 316L stainless steel in a controlled environment. The device employed for performing single track surface scans at different power (P) and scan speed (v) was the CW Laser-SEM, developed in [44]. This device is a coupling between a 1070 nm wavelength SPI QUBE 200 W CW fiber laser with a FEI Quanta 600 environmental scanning electron microscope (SEM). Additionally, the SEM is equipped with an electron backscatter diffraction (EBSD) detector. The laser power can be varied between 9 and 209 W and scanning speed between 0.01 and 20000 mm/s. The spot size can be changed from 45 to 500 µm with the help of the incorporated Scanlab varioSCANde 20i Type 133 (optical z) device. 2D scanning is possible with the equipped Scanlab intelliSCAN III 20 scanner on a relatively large area (100×100 mm^2). The laser spot size as a function of optical z and the power has been calibrated using the Femto Easy BP 13.9 beam profiler and Gentec UP55N-40S-H9-D0 calorimeter. More details on the CW Laser-SEM can be found in [44, 45].

3. Model Formulation

3.1. Thermal Multiphysics Model

The temperature distribution throughout the volume of the track is a necessary input to the PFM described above. In this section, we present the methodology employed for our multiphysics modeling, which closely follows the framework established by Samaei *et al.* [46, 47]. Key aspects of this approach, including the governing equations that represent various physical phenomena in the simulations, along with detailed information on thermophysical properties, geometric configurations, and process parameters are elucidated. To enhance model accuracy, physics relevant at the mesoscale are incorporated, including surface tension, Marangoni forces, heat loss, buoyancy, laser-material interactions, and solidification.

There are three immiscible phases in the computational domain – solid metal, liquid metal, and gas. Mass conservation is applied across the entire domain (metal and gas) to ensure that mass transfer between phases is conserved. The Volume of Fluid (VOF) method is used to differentiate metal (solid and liquid) from gas, while a temperature-dependent liquid fraction variable is employed to distinguish solid from liquid metal. To model this multiphase flow problem, mass and momentum conservation equations are solved:

$$\frac{\partial \rho}{\partial t} + \nabla \cdot (\rho \mathbf{u}) = 0 \tag{1}$$

$$\frac{\partial}{\partial t}(\rho \mathbf{u}) + \nabla \cdot (\rho \mathbf{u} \otimes \mathbf{u}) = -\nabla p + \nabla \cdot \left(\mu \left(\nabla \mathbf{u} + \nabla \mathbf{u}^T\right)\right) + \rho \mathbf{g} \beta \left(T - T_{ref}\right) - A\mathbf{u} \tag{2}$$

Here, ρ represents fluid density, $\mathbf{u}$ flow velocity, p pressure, μ fluid viscosity, $\mathbf{g}$ gravitational acceleration, β the thermal expansion coefficient, T_{ref} the reference temperature, and A the Kozeny-Carman permeability of the solid-liquid mushy zone. The last is dependent on the liquid fraction (f_L) and the characteristic length (λ_1) of the mushy region:

$$A = \frac{180\mu}{\lambda_1^2} \frac{(1-f_l)^2}{f_l^3}. \tag{3}$$

The liquid fraction linearly increases from 0 to 1 between the solidus temperature, T_S, and liquidus temperature, T_L, following the step function formulation:

$$f_L = \begin{cases} 0 & T < T_S \\ \frac{T-T_S}{T_L-T_S} & T_S < T < T_L \\ 1 & T_L < T \end{cases} \tag{4}$$

We apply the energy conservation equation to compute the temperature field within the computational domain:

$$\frac{\partial(\rho h)}{\partial t} + \nabla \cdot (\rho \mathbf{u} h) = \nabla \cdot (\kappa \nabla T) \tag{5}$$

where h and κ represent enthalpy and heat conductivity, respectively. The enthalpy is related to the temperature and the liquid fraction through the expression

$$h(T, f_L) = (1-f_L)\int_{T_{ref}}^{T} C_{p,S}(T')dT' + f_L \int_{T_{ref}}^{T} C_{p,L}(T')dT' + f_L \Delta H_{sl} \tag{6}$$

where $C_{p,S}(T)$ and $C_{p,L}(T)$ are the specific heats in the solid and liquid phases, ΔH_{sl} is the latent heat of fusion, and T_{ref} is an arbitrary reference temperature. We employ the Volume of Fluid (VOF) method to track the melt pool interface over time, with the governing equation satisfying the advection equation:

$$\frac{\partial \Phi}{\partial t} + \mathbf{u} \cdot \nabla \Phi = 0. \tag{7}$$

Here, $\Phi(x,t)$ denotes the volume fraction of metal, including both liquid and solid phases. The VOF equation is solved after the mass and momentum equations and energy equation at each timestep.

Our laser model integrates laser physics and interactions with materials. Key laser parameters, such as spot size, power, and scanning speed, are defined based on the experimental conditions. We use the ray tracing method to simulate the complex interaction between the laser and materials during the AM process [48, 49]. This approach accounts for multiple reflections influenced by the keyhole's shape.

The calculation of absorbed laser energy follows the Fresnel equation [50],

$$\alpha_{Fr}(\varepsilon, \theta) = 1 - \frac{1}{2}\left(\frac{1+(1-\varepsilon\cos\theta)^2}{1+(1+\varepsilon\cos\theta)^2} + \frac{\varepsilon^2 - 2\varepsilon\cos\theta + 2\cos^2\theta}{\varepsilon^2 + 2\varepsilon\cos\theta + 2\cos^2\theta}\right), \tag{8}$$

where α_{Fr} is the Fresnel absorptivity, θ is the angle between the laser ray incident and the normal vector of the metallic surface and ε is the material constant associated with the electrical conductance [48], respectively. For 316L, we calibrated ε to be 0.15 to match melt pool width and depth. This value is consistent with the range of 0.08–0.25 that has been reported in similar studies and leads to a zero-angle absorptivity of 25.8% [48, 51].

In the VOF formulation, heat flux at the material surface is captured through diffuse volumetric source terms in the energy equation; these include surface heating from laser interaction and heat loss due to surface convection, radiation, and evaporation. The laser beam profile is prescribed as a Gaussian profile for the incoming energy flux represented by the ray tracing method,

$$Q_{Laser} = \frac{2P}{\pi r_b^2} \exp\left(-\frac{2r^2}{r_b^2}\right), \tag{9}$$

where Q_{Laser} represents heat flux, P is the laser power, r is the radial distance from the laser beam center, and r_b is the effective radius of the laser beam, where the heat flux is $1/e^2$ of its maximum value. The total heat loss (Q_{Loss}) from the metal to the surroundings includes contributions from convection (Q_{Conv}), radiation (Q_{Rad}), and evaporation (Q_{Evap}),

$$Q_{Conv} = h_c(T - T_0), \tag{10}$$

$$Q_{Rad} = \sigma_{SB}\epsilon(T^4 - T_0^4), \tag{11}$$

$$Q_{Evap} = \frac{0.005}{\sqrt{2\pi R_v}} P_a \exp\left[\frac{\Delta H_{lv}}{R_v T_{boil}}\left(1 - \frac{T_{boil}}{T}\right)\right] \tag{12}$$

$$Q_{Loss} = Q_{Conv} + Q_{Rad} + Q_{Evap} \tag{13}$$

where h_c is the convective heat transfer coefficient, T_0 is the ambient temperature, σ_{SB} is the Stefan-Boltzmann constant, ϵ is the emissivity, ΔH_{lv} is the latent heat of evaporation, P_a is atmospheric pressure, and R_v is the gas constant for evaporated material. In the multiphysics model, surface forces play a crucial role as they provide boundary conditions for the momentum equation (the Navier-Stokes equation). These forces include the recoil pressure, responsible for creating a depression in the melt pool after the temperature of the 316L part surpasses its evaporation point, denoted as T_{boil}. Additionally, the Marangoni and capillary effects are needed due to the temperature-dependent surface tension field of 316L. Mathematically, the surface force, $\mathbf{F}_{Surf}$ can be expressed as

$$\mathbf{F}_{Surf} = \gamma_{LV}\kappa\mathbf{n} + (\nabla T - \mathbf{n}(\nabla T \cdot \mathbf{n}))\frac{\partial \gamma_{LV}}{\partial T} - P_{\text{recoil}}\mathbf{n} \tag{14}$$

$$P_{\text{recoil}} = 0.54 P_\alpha \exp\left(\frac{\Delta H_{lv}}{R_v T_{\text{boil}}}\left(1 - \frac{T_{\text{boil}}}{T}\right)\right) \tag{15}$$

where γ_{LV} is the liquid-vapor surface tension at surface temperature T, κ is the total curvature of the exposed 316L metallic phase surface, $\mathbf{n}$ is the normal vector to the free surface, ∇T is the temperature gradient, and $\left(\frac{\partial \gamma_{LV}}{\partial T}\right)$ is the sensitivity of 316L surface tension to temperature.

3.2. Microstructure Model

The temperature distribution is a necessary input to predict the microstructural evolution with a phase-field model. Here, we employ a PFM developed for polycrystalline solidification under AM conditions in systems that solidify in a planar or low-amplitude cellular regime [34, 36, 37]. The assumption is consistent with self-consistent thermodynamic calculations of the interfacial temperature during solidification of 316L recently performed by Martin et al. [52], which predict that planar solidification is likely under steady-state conditions at the velocities and thermal gradients encountered in this study. This contrasts with the slower velocities and lower gradients that are more characteristic of laser welding that typically produce dendritic growth [53–55], although the present PFM predicts columnar grain morphologies that are similar to those observed in laser welds [34]. In the planar and low amplitude cellular regimes, trijunctions on the solid-liquid interface are assumed to be sufficiently mobile such that the resulting grain boundary is perpendicular to the solid-liquid interface [34, 56]. We present an abbreviated description of the governing equations of the PFM. Additional details on the model development, its expected behaviors, and its analytical verification are available in the previous studies [34, 36, 37].

The PFM is derived from a functional of the total Helmholtz free energy of the system, $\mathcal{F}$,

$$\mathcal{F} = \int_V \left[f(\{\phi\}, T) + \frac{\kappa}{2}\sum_{i=0}^{N}|\nabla\phi_i|^2\right] dV, \tag{16}$$

where $\{\phi\}$ is a set of nonconserved order parameters that represent the melt pool and individual crystallographic orientations in the solid, T is the absolute temperature, κ is a gradient energy coefficient, and N is the number of solid order parameters. The homogeneous free energy density, $f(\{\phi\}, T)$, contains contributions from a multiwell energy density and the latent heat of fusion,

$$f(\{\phi\}, T) = W\left[\sum_{i=0}^{N}\left(\frac{\phi_i^4}{4} - \frac{\phi_i^3}{3}\right) + \frac{1}{2}\sum_{i=0}^{N}\sum_{j>i}^{N}\phi_i^2\phi_j^2 + \frac{1}{12}\right] + L_v\frac{T_L - T}{T_L}h(\{\phi\}), \tag{17}$$

where W is the height of the multiwell, L_v is the volumetric latent heat of fusion, T_L is the liquidus temperature, and $h(\{\phi\})$ is a 6th-order Moelans-type interpolation function with a value of zero in the solid and one in the liquid [36, 57, 58]. Each order parameter evolves according to an Allen-Cahn-type equation,

$$\frac{\partial \phi_i}{\partial t} = -M(\{\phi\}, T)\frac{\delta \mathcal{F}}{\delta \phi_i}, \tag{18}$$

where $M(\{\phi\}, T)$ is the local mobility of the order parameter, which is locally interpolated according to the pairwise values of order parameters and interfacial mobilities [34, 59].

Generally, the expressions relating the phase-field parameters to their sharp interface equivalents are the same as in previous work [34, 36, 37]. The values of W and κ are related to the diffuse interface thickness, ζ, and solid-liquid interface energy, γ_{SL}, as

$$W = \frac{6\gamma_{SL}}{\zeta}, \tag{19}$$

$$\kappa = \frac{3\gamma_{SL}\zeta}{2}. \tag{20}$$

Note that we do not assign different energies to grain boundaries. The orientation-dependent solid-liquid interface mobility is assumed to follow a two-parameter cubic harmonic expansion,

$$M_{SL}(\mathbf{n}_{ij}) = \frac{2T_L\mu_0}{3\zeta L_v}\left[1 + \epsilon_4\left(4\sum_{k=1}^{3} n_{ij,k}^4 - 3\right)\right], \tag{21}$$

where μ_0 is the modulus of the solid-liquid mobility, ϵ_4 is the anisotropy parameter, and $n_{ij,k}$ is the k-th component of the normal vector between order parameters i and j. Presently, μ_0 is assumed to be constant, but the effects of microsegregation during solidification could be included through a nonlinear relationship of velocity and undercooling [52]. Where $\partial T/\partial t > 0$, we define an isotropic mobility of the melting interface,

$$M_{melt} = \frac{4T_L\mu_0}{3\zeta L_v}, \tag{22}$$

which prevents numerical pinning. Additionally, along melting interfaces we halve the latent heat term of the Allen-Cahn equation to maintain the correct interface velocity; thus the increased mobility can also be interpreted as an increase in the interfacial energy, which is well-known to numerically stabilize phase-field models. Finally, we relax our previous assumption that grain boundary motion is negligible and introduce an Arrhenius-type behavior for thermally activated grain boundary mobility,

$$M_{GB}(T) = A_0 \exp\left[-\frac{Q_{GB}}{RT}\right], \tag{23}$$

where A_0 is the mobility prefactor, Q_{GB} is the activation energy, and R is the ideal gas constant. Thus, as the temperature increases in proximity to the melt pool, the grain boundary mobility will increase. The prefactor is chosen such that the grain boundary mobility is comparable to the solid-liquid mobility at the liquidus temperature,

$$A_0 = \frac{2T_L\mu_0}{3\zeta L_v}\exp\left[\frac{Q_{GB}}{RT_L}\right]. \tag{24}$$

The above pairwise mobilities give the overall interpolated mobilities for the Allen-Cahn equation,

$$M(\{\phi\}, T) = \frac{\sum_{i=0}^{N}\sum_{j>i}^{N}\phi_i^2\phi_j^2 M_{ij}}{\sum_{i=0}^{N}\sum_{j>i}^{N}\phi_i^2\phi_j^2}, \tag{25}$$

$$M_{ij} = \begin{cases} M_{SL}(\mathbf{n}_{ij}) & (i = 0 \vee j = 0) \wedge \partial T/\partial t \leq 0, \\ M_{melt} & (i = 0 \vee j = 0) \wedge \partial T/\partial t > 0, \\ M_{GB}(T) & i \neq 0 \wedge j \neq 0. \end{cases} \tag{26}$$

3.3. Numerical Details and Simulation Design

In this study, the PFM and thermal multiphysics model are solved asynchronously. First, thermal-fluid simulations are conducted using FLOW-3D® to replicate experimental setups [60]. The simulations focus on a single configuration involving a moving laser applied to solid substrates. Nine distinct simulations are performed to match the considered experimental conditions, each varying in laser power and scanning speed. A 3D simulation domain is created with dimensions of 500 µm (x/scan direction) by 200 µm (y/transverse direction) by 130 µm (z/normal direction) for simulating thermal multiphase flow in a given single track. To facilitate accurate simulations, a structured mesh is employed, comprising 3 µm × 3 µm × 3 µm cubic cells. For all cases, the model included a total of 481,127 mesh cells. A mesh sensitivity analysis was performed by using different voxel sizes, and the melt pool size was found to change by approximately 1% at steady state between 3- and 4-micron meshes. This minimal difference indicates that the chosen voxel size is sufficient for accurately capturing the melt pool curvature without distorting the results.

The laser is moved along the positive x-axis, spanning from coordinates $(x, y) = (50\,\mu\text{m},\ 100\,\mu\text{m})$ to $(440\,\mu\text{m},\ 100\,\mu\text{m})$ to form the track on the solid substrate. The material properties used for the simulations are listed in Table 3. In Flow-3D, the VOF method is solved with a finite volume discretization of the momentum and continuity equations while tracking the interface between different phases. Time integration of the pressure and heat transfer equations is performed implicitly, and the resulting system of equations is solved by the Generalized Minimal Residual (GMRES) method. The calculation of the free surface pressure and surface tension pressure employ explicit methods to capture the effects of these phenomena on fluid flow behavior. A total of 2,930 core hours was required to perform the simulations for melt pool Tracks 1–9, although the computational cost varied based on the specific parameters of a track.

Property	**Definition**	**Value**	**Units**
ρ_S	Density in solid phase [61]	$8084.2 - 0.42086T - 3.8942 \times 10^{-5}T^2$	kg/m^3
ρ_L	Density in liquid phase [61]	$7432.7 + 0.039338T - 1.8007 \times 10^{-4}T^2$	kg/m^3
μ	Viscosity [61]	$\exp\left(-0.5958 + \frac{2385.2}{T}\right) \times 10^{-3}$	mPa s
$C_{p,S}$	Heat capacity in solid phase [61]	$458.98 + 0.1328T$	J/(kgK)
$C_{p,L}$	Heat capacity in liquid phase [61]	769.86	J/(kgK)
κ_S	Thermal conductivity in solid [61]	$9.248 + 0.01571T$	W/(mK)
κ_L	Thermal conductivity in liquid [61]	$12.41 + 0.003279T$	W/(mK)
h_c	Convective heat transfer coefficient [62]	25	W/(m^{2}K)
ΔH_{sl}	Latent heat of fusion [61]	2.677×10^2	kJ/(kg)
ΔH_{lv}	Latent heat of evaporation [61]	7.416×10^3	kJ/(kg)
T_S	Solidus temperature [63]	1674.15	K
T_L	Liquidus temperature [63]	1697.15	K
T_{boil}	Boiling temperature [63]	3090	K
R_v	Gas constant	1.50774×10^6	cm^2/(s^{2}K)
ε	Electrical conductance parameter	0.15	
γ_{LV}	Liquid-vapor surface tension [64, 65]	$1544.01 - 0.1988(T - 1674)$	mN/m
γ_{SL}	Solid-liquid interfacial energy [66, 67]	0.25	J/m^2
ζ	Diffuse interface length scale	408	nm
μ_0	Solid-liquid mobility modulus [67]	0.217	m/sK
ϵ_4	Solid-liquid mobility anisotropy [36, 67]	0.3	
L_v	Volumetric latent heat of fusion [61, 66]	1.3	kJ/cm^3
Q_{GB}	Grain boundary activation energy [68, 69]	150	kJ/mol

Table 3: Materials properties of 316L used in the simulations. When multiple references are reported for a parameter, the employed value is chosen from within the range of values that have been reported.

The thermal multiphysics model requires a different numerical mesh resolution than the PFM. Therefore, the calculated temperature profile must be interpolated onto the mesh of the PFM. We employ a modification of the method described by Saye [70], where polynomials of a fixed order are fit to a stencil of the finite volume mesh by least-squares approximation. Here, we employ a second-order Taylor polynomial,

$$T(x,y,z) = c_0 + c_1x + c_2y + c_3z + c_4x^2 + c_5y^2 + c_6z^2 + c_7xy + c_8xz + c_9yz, \tag{27}$$

where the c_i are the coefficients of the polynomial. When Eq. 27 is fit to a subset of the overall mesh, the resulting system of equations can be written and solved as

$$\vec{T} = \mathbf{A}\vec{c}, \tag{28}$$

$$\vec{c} = \left(\mathbf{A}^T\mathbf{A}\right)^{-1}\mathbf{A}^T\vec{T} \tag{29}$$

where $\vec{T}$ is a column vector of the temperatures in the smaller fitting stencil, $\mathbf{A}$ is a Vandermonde matrix representation of Eq. 27, and $\vec{c}$ is a column vector of the unknown coefficients. The matrix inversion in Eq. 29 can be analytically precalculated for a desired polynomial and stencil, which dramatically increases the efficiency of the reconstruction. We find that fitting Eq. 27 to a $4\times4\times4$ stencil of the temperature solution balances the computational cost of the interpolation while maintaining the fidelity of the interpolated output. This combination of polynomial and stencil size also provides a degree of smoothing to the temperature profile that stabilizes the numerical solution of the PFM.

The governing equations for the PFM are implemented in a custom numerical framework. A nonlinear transformation is applied to Eq. 18 for each order parameter field [34, 36, 37, 71], which creates a set of governing equations for the signed distance fields describing interface locations rather than the original order parameters. The transformed versions of the governing equations are available in Ref. [36] and are omitted here for conciseness. This nonlinear transformation also allows for coarser numerical meshes to be employed than is needed for the solution of the untransformed PDE. The governing equations are then solved by the method of lines using an isotropic, second-order, cell-centered finite difference spatial discretization and an adaptive third-order explicit Runge-Kutta time integration method [72, 73]. The overall framework is implemented primarily in Fortran 2008 and is parallelized with MPI. To reduce memory usage, we employ 16 total order parameters with a variant of the active parameter tracking (APT) method [74, 75], which is modified to accommodate adaptive time stepping. All calculations employed a $1600 \times 768 \times 384$ mesh with a uniform mesh spacing of 240 nm. While this mesh is coarser than in [34], the expected solidification behaviors were found to be equivalent in following studies [36, 37]. The parameters employed for the PFM are also listed in Table 3. Here, the chosen value of ζ results in an interface that has a typical width of eight grid points and matches the ratio of ζ to grid spacing employed in previous studies [34, 36, 37]. The grain boundary activation energy is chosen to be within the reported range of 135–316 kJ/mol for 316L and similar austenitic stainless steels [68, 69].

As implemented, the two models are coupled in a one-way manner. After the thermal multiphysics model attains a quasi-steady-state condition, the temperature field is exported from FLOW-3D and minimally post-processed into a format that can be read by the PFM. During the startup of the PFM framework, a lookup table (LUT) is created from the FLOW-3D solution that can be employed in the least-squares interpolation described above. Each task in the parallel domain decomposition only requires a small fraction of the overall LUT; thus, the LUT is cropped to the smallest necessary size for each task to reduce memory usage. Although surface forces are always included in the VOF simulations, the resulting deformation is generally small and does not significantly affect the overall melt pool shape. Additionally, the PFM employed in this study does not consider the vapor phase. Thus, we neglect the surface deformation that is present in the steady-state melt pools obtained from VOF when generating the LUTs for the PFM. This simplification allows for more efficient modeling without sacrificing the accuracy of the results.

Production simulations were run across 1,024 cores on both Anvil at Purdue University and Quest11 at Northwestern University, with the shortest simulation running for approximately 4 days and the longest running for approximately 14 days. The overall computational cost was approximately 830,000 core hours to perform the PFM simulations for Tracks 5–9. Tracks 1–4 would require significantly more time and/or memory due to their higher energy densities, slow scanning speeds, and resulting melt pool sizes; therefore, these tracks are not calculated in the present study.

Track ID	**Pool Depth** (µm)	**Pool Width** (µm)
1	152.52	146.71
2	30.64	82.2
3	110.3	119.39
4	25.14	76.07
5	14.16	51.56
6	40.78	79.87
7	12.26	50.29
8	18.59	55.78
9	10.57	39.72

Table 4: Measured melt pool dimensions.

3.4. Initial Condition Generation

The microstructural evolution in response to laser remelting is simulated for a polycrystalline volume of material. A common synthetic initial condition is generated that is subsequently employed for each set of experimental conditions. From EBSD analysis of the experimental baseplate prior to lasering, we first identify grains and merge twins with their parent orientations using MTEX [76]. We determine the grain size distribution of the merged microstructure, assuming the mean intercept area of a sphere is $\bar{A} = 2\pi r^2/3$ [77]. The grain size distribution as measured on the surface is well-described by a lognormal distribution with $\mu = 2.84$ and $\sigma = 0.49$, which produces an average equivalent sphere diameter of 19.3 µm. In addition, we obtain a weighted histogram of the averaged crystallographic orientations of each grain to approximate the orientation distribution function (ODF) of the baseplate. The grain size distribution and ODF are combined into a pipeline in DREAM.3D [78], which is used to generate the initial condition for the simulations. After generation, coherent $\Sigma 3$ twin boundaries are randomly inserted into the microstructure to be consistent with the experimental microstructure. However, in the present work, these twins exist only to introduce variations in the solid-liquid interface mobility and the grain morphologies encountered during the melting and resolidification processes. No special properties (e.g., low energy or mobility) are introduced to the twin boundaries, and a comprehensive examination of the role of twin boundaries on the microstructural evolution is beyond the scope of the present study.

4. Results and Discussion

4.1. Experimental Results and Multiphysics Model Calibration

The EBSD scans performed before and after the laser passes inside the CW Laser-SEM are shown in Fig. 1. The state before melting can be observed in Fig. 1a. After laser scanning, preexisting grains grow epitaxially towards the melt pool center (Fig. 1b), bending to follow the laser scanning direction and the consequent temperature gradient.

Detailed views of the marked regions in Fig. 1 are presented in Fig. 2 for before (a–c) and after (d–f) the laser scan. We observe instances where preexisting twin boundaries in the plate change orientation and solidify across the melt pool boundary, as exemplified by the circled grains in Fig. 2d–f when compared with the initial regions in Fig. 2a–c. The influence of power can be appreciated when observing Fig. 2d–f; for these three tracks the scanning speed is the same, $500\,\mathrm{mm\,s^{-1}}$, but power is 66, 45 and 24 W, respectively.

Melt pool dimensions are obtained from the EBSD scans and optical microscopy on both the surface and the cross-section. The cross-section is obtained by cutting the sample after lasering; the subsequent surface preparation and characterization steps are the same as those employed for characterization of the top surface prior to the laser scans. Additionally, all CFD simulations were run until steady-state conditions were achieved, where melt pool depths and widths remained constant. The depths and widths of the melt pools within these steady-state conditions (see Fig. 3) were measured for all cases. The measured melt pool depth and width are listed in Table 4. Notably, Tracks 1 and 3 appear to be in keyhole mode based on the significant increase in melt pool width and depth. Whereas the width of the melt pool is approximately 2-4 times the depth for the tracks in conduction mode, Tracks 1 and 3 are have widths that are comparable to their depths.

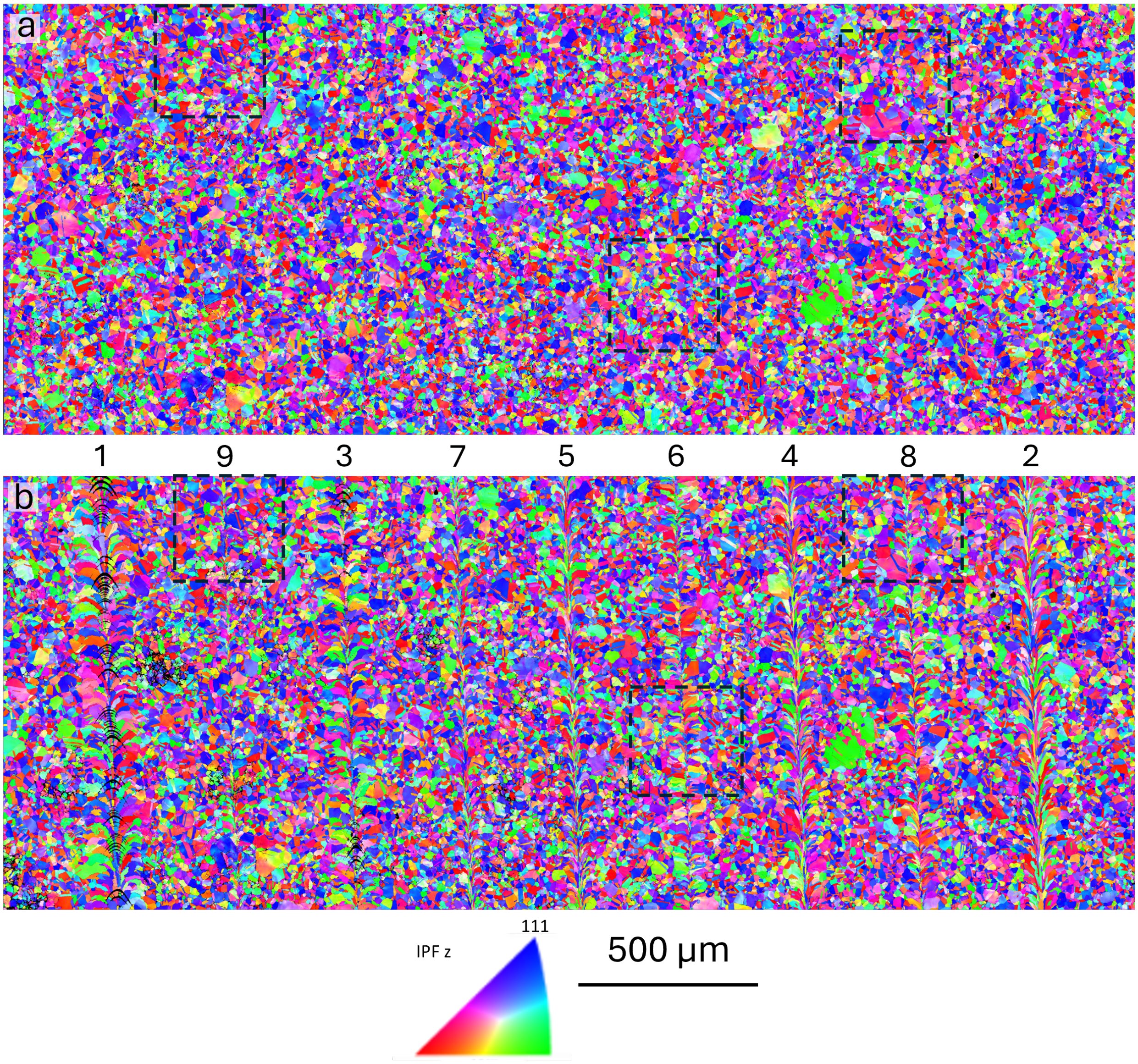

Figure 1: EBSD of wrought and annealed 316L before (a) and after the laser pass (b). The IPF color is in the out-of-plane direction. The marked regions in (a) are the detail areas shown in Fig. 2.

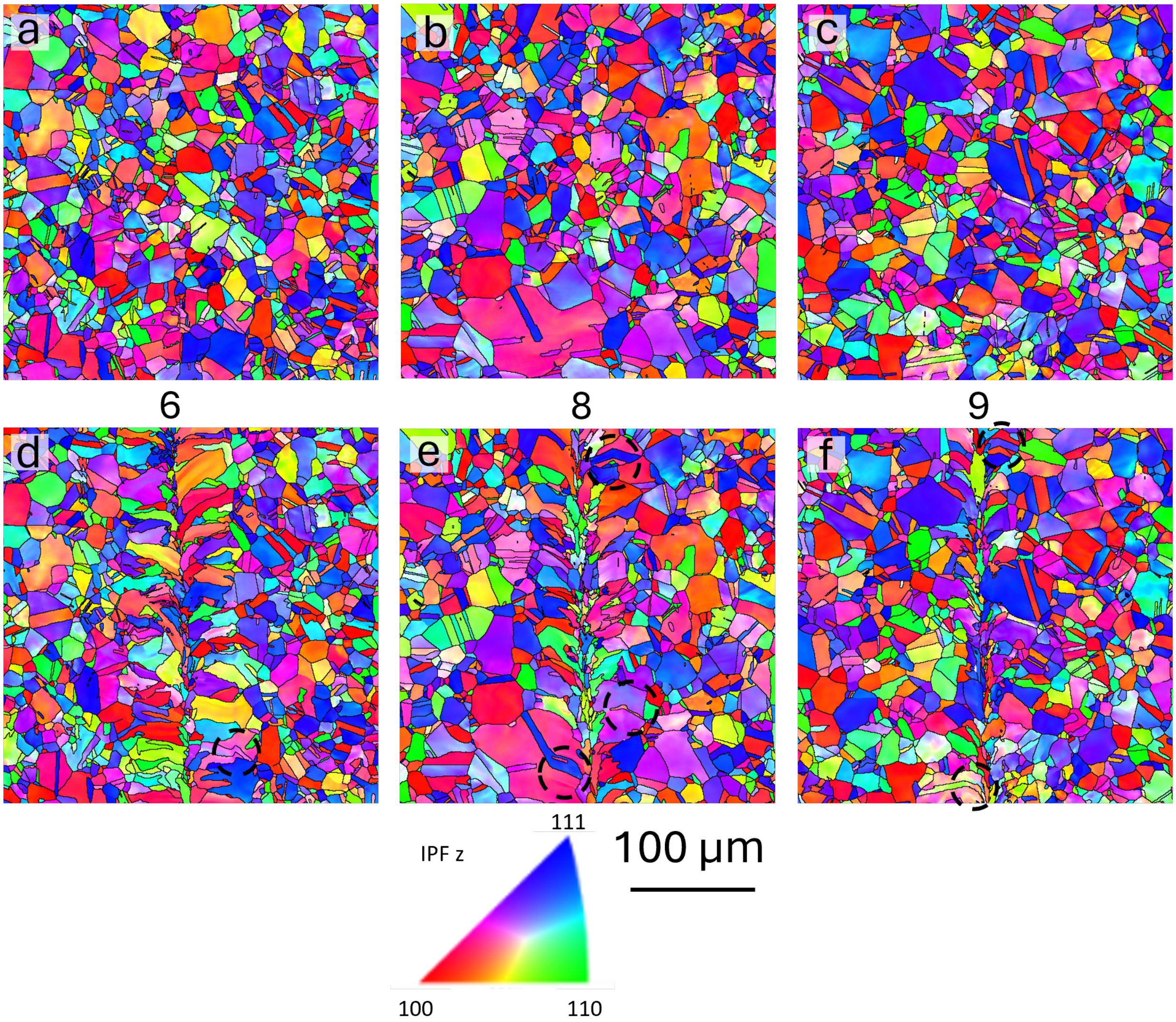

Figure 2: Detail (marked in Fig. 1a) of 500 mm s^{-1} tracks 6 (a,d), 8 (b,e) and 9 (c,f) before (a–c) and after (d–f) the laser pass. The IPF color is in the out-of-plane direction. The circled grains in (d–f) are examples where a twin boundary changed directions during solidification.

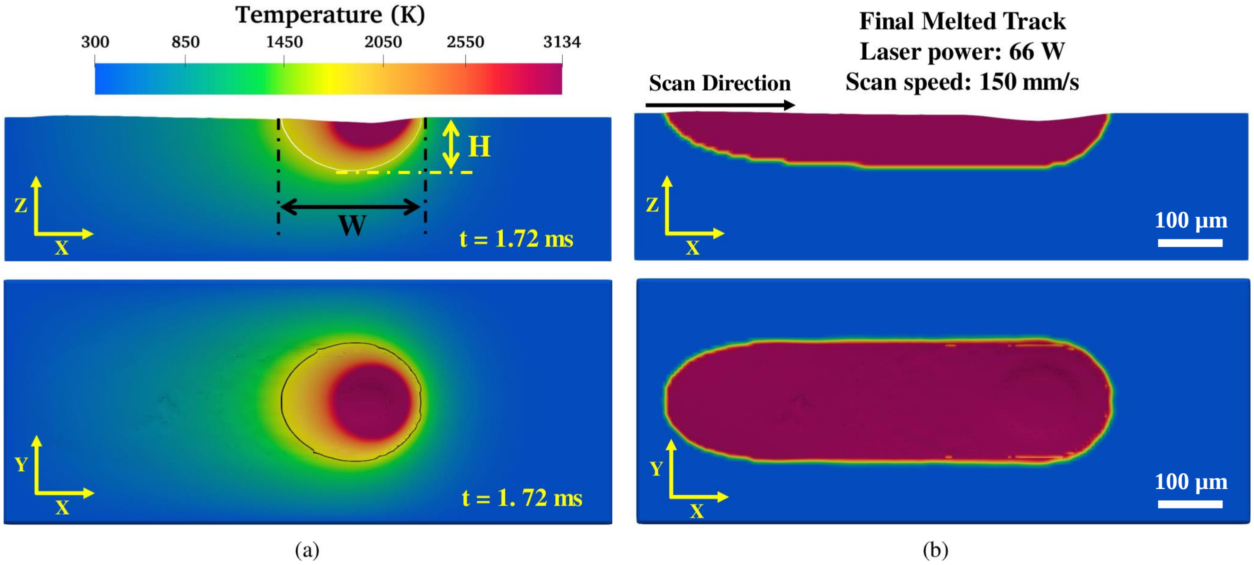

Figure 3: Thermal-fluid simulation results for temperature distribution and track geometry. (a) Cross-sectional (top) and top-down (bottom) views of temperature distributions at $t = 172\,\text{ms}$, representing the steady-state state of the melt pool. White and black lines in the top and bottom plots respectively indicate the melt pool interface. The geometry of the melt pool is defined by depth (H) and width (W) as illustrated in the top view. (b) Cross-sectional (top) and top-down (bottom) views of the final resolidified track. The red region represents areas that underwent melting during the process, while the blue region remained unaffected.

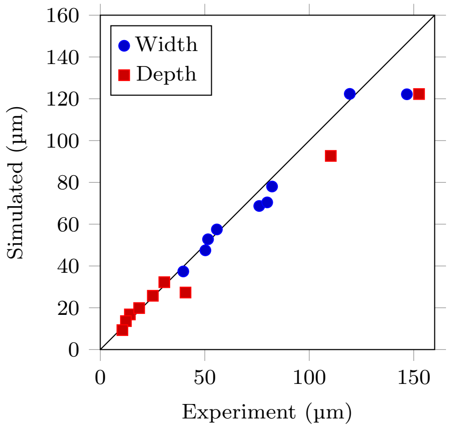

Figure 4: Comparison of the experimentally measured melt pool dimensions and those predicted by the thermal-fluid simulations.

The experimental melt pool dimensions are obtained from EBSD measurements of the cross-section of the sample, while the dimensions of the simulated melt pools are calculated from the isosurface of the liquidus temperature from the thermal multiphysics simulations. In both cases, the depth is calculated relative to the flat surface of the surrounding unmelted regions. The melt pool dimensions of the experiments and simulations are compared in Fig. 4, with the width and depth plotted as blue circles and red squares, respectively. If we fit a line through the origin, the resulting slopes are 0.823 for the depth and 0.923 for the width. While these indicate a slight underprediction of the melt pool dimensions, it seems to be characteristic of the 66 W conditions of Tracks 1, 3, and 6. This suggests that the absorptivity (ε in Eq. 8) of the liquid phase increases at higher power densities beyond any effective increase from internal reflections in the melt pool. If we consider only the 24 W and 45 W data, the linear slopes for the depth and width are 1.05 and 0.956, respectively. Additionally, if we fit a power law relationship (not shown) between the depth (d) and width (w), we obtain $w = 14.2d^{0.468}$ for the experiments and $w = 16.0d^{0.442}$ for the simulations. Thus, we observe good agreement between the simulated and measured dimensions for all melt pools in conduction mode.

4.2. Comparison of Experimental and Simulated Top-Surface Grain Morphologies

We compare the predicted microstructures of the top surface for each of the PFM simulations of Tracks 5–9 against their corresponding experiments in Fig. 5. The laser power for Tracks 5, 7, and 9 is fixed at 24 W, while the scan velocity is fixed at 500 mm/s for Tracks 6, 8, and 9. Therefore, we are able to observe the effects of increasing either the power or velocity on the obtained microstructure: Track 9 is shared between the two sets. Visually, we observe qualitative agreement between the simulated and experimental microstructures.

At the lowest velocity of 150 mm/s (Track 5, Fig. 5), the resolidified features develop a characteristic curved appearance with respect to the center of the laser track. This is similar to the feather- or frond-like morphology observed in PFM simulations and other experiments [34, 36–38, 79–81]. Grains begin solidifying at the sides of the melt pool and curve as they follow the melt pool surface [34]. Towards the centerline, competitive grain growth from variations in the solid-liquid mobility and the Gibbs-Thomson effect eventually cause slender, unfavorably aligned grains to be overgrown by their neighbors, ending solidification. The grains that outcompete their neighbors progressively align with the scan direction, and along the center of the laser track there is a combination of these kinetically favorable grains and small features belonging to grains that likely grew upward from the bottom of the melt pool.

As the scan velocity is increased to 250 mm/s (Track 7, Fig. 5) and 500 mm/s (Track 9, Fig. 5), we observe two primary effects. First, as the melt pool decreases in width and depth the set of grains that melt and resolidify becomes smaller. In the simulations, we observe grains in Tracks 7 and 9 that are absent in Track 5. These grains are located such that they fully melted or coarsened at the lower velocity, but were able to survive and resolidify at the higher velocities. Second, the grains that do resolidify become less noticeably curved in the scan direction, although small features remain visible along the center of the laser tracks that belong to grains lower in the melt pool. We note that, for the fastest velocity where the grains are minimally curved, the melt pool depth is comparable to the grain size of the input microstructure. Conversely, previous simulations where the grain size is smaller than the dimensions of melt pool produced grains with significant curvature [34]. This suggests that there may be a characteristic length scale for a combination of melt pool dimensions and grain size that determines whether strongly curved grains will form in a given laser pass. However, the prior study notably did not consider the effects of twinning, and therefore a comprehensive exploration of this possibility is beyond the scope of the present work.

For Tracks 9, 8, and 6 in Fig. 5, we observe that progressively more grains melt and resolidify as the melt pool width and depth increase with the laser power. However, rather than becoming significantly more curved, the angle of the initial growth direction of grains near the sides of the track approaches $\pi/2$ to the scan direction, i.e., the grains initially grow nearly perpendicular to the scan direction. In the experiments, this eventually causes the grains to "collide" with each other along the center of the track in Track 6. By comparison, a few very slender grains survive in the simulated Track 6 along the scan direction. While this is not observed in the experiment, the narrow length scale of these simulated grains should make their evolution particularly sensitive to small perturbations of the melt pool shape. Thus, a deviation in the local melt pool shape or the solidification kinetics would likely cause these grains to be overgrown at significantly earlier times. This effect may be observed through some combination of a two-way coupling of the PFM

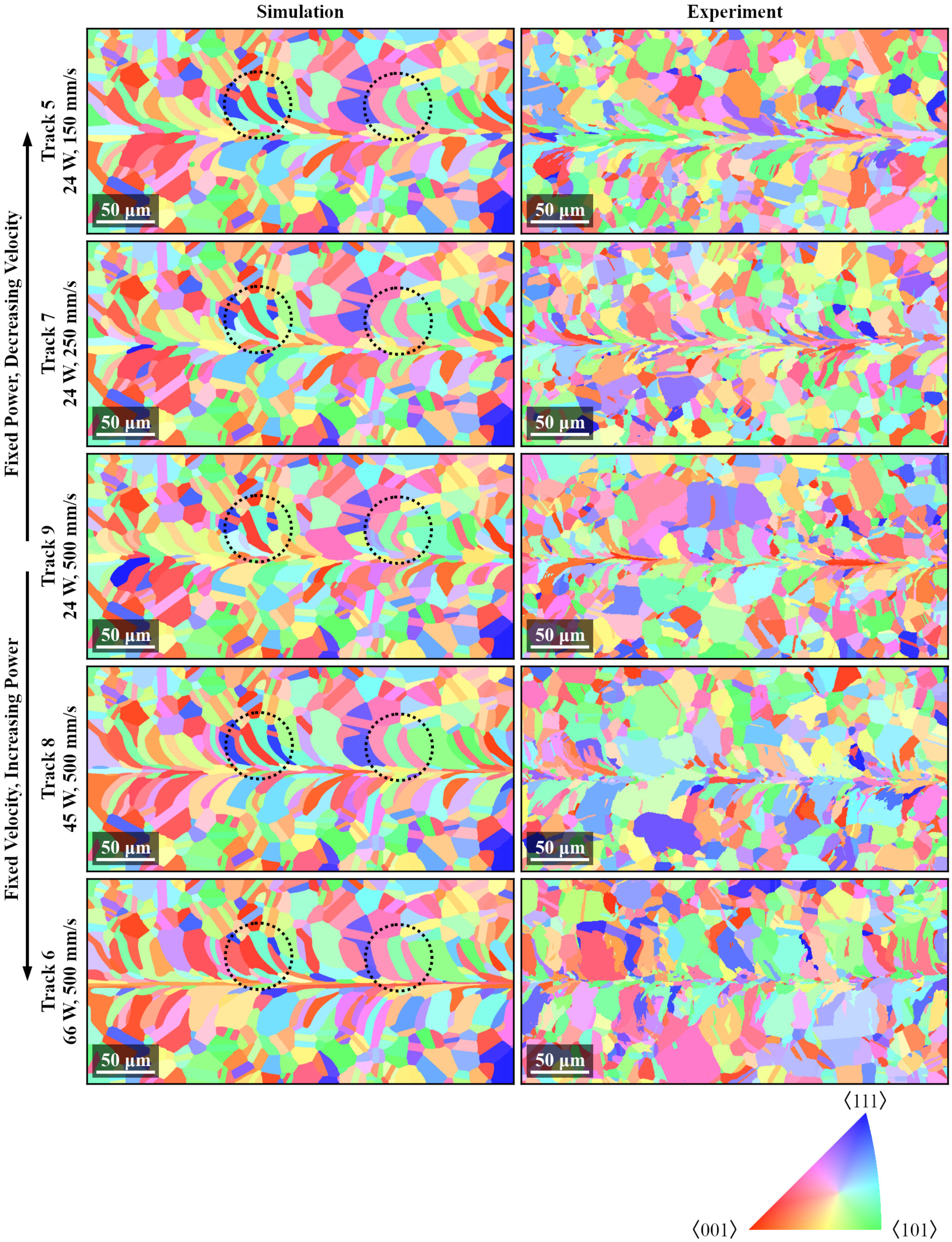

Figure 5: Comparisons of the top surface microstructure between the simulation framework (left column) and experiments (right). Tracks 5, 7, and 9 share a laser power of 24 W, while Tracks 6, 8, and 9 share a scan velocity of 500 mm/s. IPF coloring assumes ⟨001⟩ is parallel to the scan direction. The dashed circles on the simulated microstructures indicate two of the twinned grains present in all datasets.

and thermal model to consider local variations in the latent heat release, including white noise in the PFM on the order of typical thermal fluctuations, or by modifying the kinetic model to consider the effects of microsegregation on the undercooling.

Across the simulations, we frequently observe that twinned grains resolidify such that both the parent grain and its twin solidify in the same general direction. Thus, while twins introduce additional high-mobility solidification directions to the system, there is not necessarily a direct correlation between the twinned crystallographic orientations and the direction in which they solidify. For example, the circled teal-red and magenta-green grains in the simulations in Fig. 5 have different morphologies in each track due to the change in the melt pool shape, which affects the competitive resolidification. The parent teal and magenta grains have high-index crystallographic directions aligned with the scan direction, while the red and green twins have approximately $\langle 100\rangle$ and $\langle 110\rangle$ directions close to the scan direction, respectively. Despite differences in the expected interfacial mobilities, the parent and twin solidify at similar relative angles to the scan direction. Note that this behavior is also observed in the experiments (cf. Fig. 2 and accompanying discussion). Additionally, the presence of the twin affects the competition between neighboring grains. For example, the yellow grain to the right of the teal-red grain is able to cutoff the teal portion of the grain in Track 9, but the teal grain competes more effectively in Track 7.

In addition to the qualitative comparison of the microstructures, we compare quantitative aspects of their morphological features. For a given PFM microstructure, connected features are identified by obtaining a list of orientations IDs that share first- or second-nearest-neighbor pixels in the top surface slice. Any two orientation IDs that are connected are subsequently merged into a single parent grain if the misorientation between them satisfies the Brandon criterion for a $\Sigma 3$ twin boundary [82]. These merged grains are then compared against the grains that were identified in the experimental dataset after laser exposure (cf. Sec. 3.4). We calculate the major and minor axes lengths of the bounding ellipses, their orientation with respect to the scan direction, and the aspect ratio of each feature using the scikit-image Python package [83]. We filter both the experimental and simulated datasets to only consider grains where the fitted minor axis length is greater than 32ζ. Below this length scale, the dynamics of grains in the PFM are sensitive to the interface thickness ($\propto \zeta$) and the coordination of a grain with its neighbors, and therefore may not exactly match the expected sharp interface behavior [84].

The empirical cumulative distribution functions (ECDFs) of the obtained morphological quantities are plotted in Fig. 6. Each column of Fig. 6 corresponds to a single track. Within a row, the ECDFs are plotted for a given morphological quantity. The 95% confidence intervals of the simulated ECDFs are estimated from the Kolmogorov-Smirnov test statistic, $F(x) \pm [\ln(2/\alpha)/2n]^{1/2}$, where $\alpha = 0.05$ and n is the number of points in the ECDF [85]. More robust quantification of these bounds would carry substantial computational cost. Generally, we observe good agreement between the experimental datasets (black lines with markers) and the simulated datasets (solid red lines): the distance between the ECDFs is either minimal, or the experimental curve is contained within the confidence intervals of the simulations (dotted black lines). For the major and minor axes lengths (Fig. 6a and b), the experiments generally have longer maximum grain lengths than observed in the simulations, but it is unclear how much of this is due to the finite sample size of the PFM or other uncertainties in the model inputs such as the simulated melt pool dimensions. The change in grain curvature that is visible in Fig. 5 is readily apparent in the ellipse orientations (Fig. 6c). As defined, an orientation of 0 occurs when the major axis of a bounding ellipse is parallel to the scan direction. Thus, an increase in the number of grains located towards $\pm\pi/2$ indicates that more grains are aligned with the transverse direction, i.e., the grains appear to be oriented closer to the normal to the scan direction. We observe such an increase as we move outward from Track 9; Tracks 8 and 6, in particular, have very noticeable increases at the edges of the distribution. If we now consider the aspect ratios of the bounding ellipses (plotted as their inverse in Fig. 6d), we again observe good agreement between the simulations and experiments. For the considered experiments and simulations, most of the features observed on the top surface are not circular (i.e., the inverse aspect ratio is less than one), and both sets of data display a roughly sigmoidal shape of the ECDF. Overall, we conclude that the simulated microstructures reproduce key features of the experimental microstructures.

4.3. Three-Dimensional Analysis of Predicted Microstructures

In addition to the 2D comparisons against experiment, the grains of the overall 3D simulation datasets are also analyzed. As in the previous section, connected features whose misorientation satisfies the Brandon

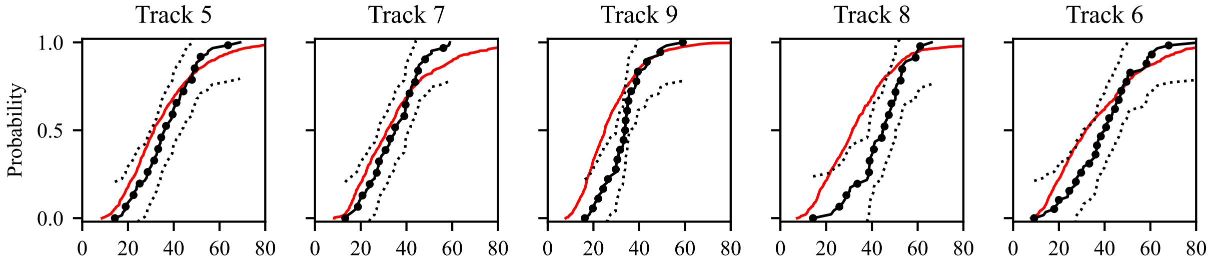

(a) Major Axis Length (μm)

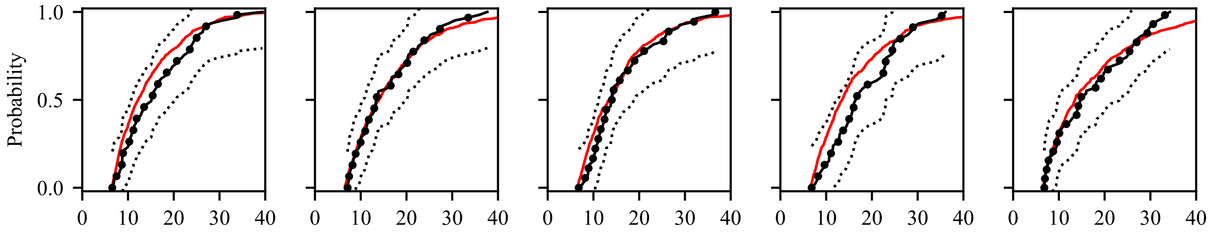

(b) Minor Axis Length (μm)

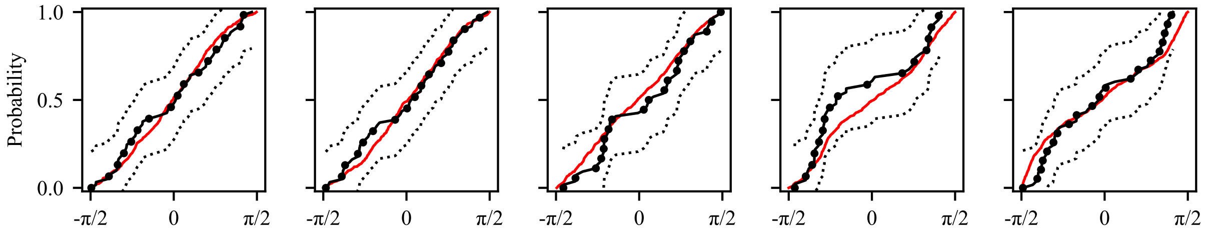

(c) Orientation

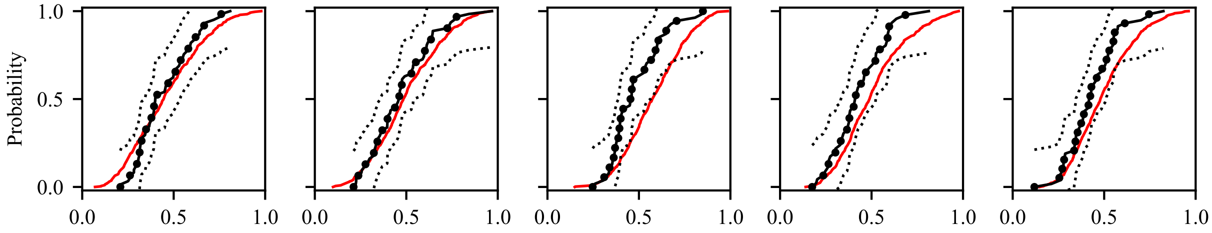

(d) Inverse Aspect Ratio

Figure 6: Comparisons of two-dimensional morphological features of the melted and resolidified grains in the experimental (red lines) and simulated (black dotted lines) datasets: (a) major and (b) minor axis lengths of the bounding ellipses, (c) orientation of the bounding ellipses, and (d) inverse aspect ratio of each grain. The columns are organized to be consistent with the rows of Fig. 5. The black dotted lines are estimated 95% confidence intervals.

criterion for a coherent $\Sigma3$ twin are merged into unified grains [82]. Only grains that completely solidified during the simulation and do not touch the ends of the simulation domain in the scan direction are retained for further analysis, but no additional filtering by grain size is performed. For each of the identified grains, we then calculate the second order central moment tensor (the moment of inertia tensor) of the grain [86],

$$\mathcal{I}_n = \begin{pmatrix} \mu_{020} + \mu_{002} & -\mu_{110} & -\mu_{101} \\ -\mu_{110} & \mu_{200} + \mu_{002} & -\mu_{011} \\ -\mu_{101} & -\mu_{011} & \mu_{200} + \mu_{020} \end{pmatrix}. \tag{30}$$

Here,

$$\mu_{ijk} = \int_V (x - \bar{x}_n)^i (y - \bar{y}_n)^j (z - \bar{z}_n)^k g(\mathbf{r}) dV \tag{31}$$

are the corresponding moments with respect to the centroid of grain n, where $g(\mathbf{r})$ is 1 inside a grain and 0 outside a grain. If we perform an eigendecomposition, $\mathcal{I}_n = \mathbf{Q}_n \mathbf{\Lambda}_n \mathbf{Q}_n^{-1}$, the principal axes of the grain are the columns of the matrix $\mathbf{Q}_n$. The eigenvalue matrix, $\mathbf{\Lambda}_n$, is the moment tensor in the principal axes coordinates,

$$\mathbf{\Lambda}_n = \begin{pmatrix} \tilde{\mu}_{020} + \tilde{\mu}_{002} & 0 & 0 \\ 0 & \tilde{\mu}_{200} + \tilde{\mu}_{002} & 0 \\ 0 & 0 & \tilde{\mu}_{200} + \tilde{\mu}_{020} \end{pmatrix}. \tag{32}$$

Here, $\tilde{\mu}_{ijk}$ are the central moments in the rotated coordinate system represented by $\mathbf{Q}_n$, i.e, if the principal axes are known for a grain, then $\tilde{\mu}_{ijk}$ can be calculated directly from Eq. 31 in the rotated frame. Therefore, we may obtain the semi-axes lengths of the equivalent ellipsoid as $a = (5\tilde{\mu}_{200}/V)^{1/2}$, $b = (5\tilde{\mu}_{020}/V)^{1/2}$, $c = (5\tilde{\mu}_{002}/V)^{1/2}$, where V is the grain volume. Multiplying each of these by two gives the overall length of the axes.

The ECDFs of the calculated axes lengths for the simulations are plotted in Fig. 7. Additionally, we include the CDF of the input lognormal grain size distribution (cf. Sec. 3.4) for reference, but truncate it to an upper bound of 37.4 µm to align with the largest feature size represented in the DREAM.3D pipeline. We immediately observe that only the major axis (7a) varies significantly from one track to another. Track 6 (66 W, 500 mm s^{-1}) produces the longest grains on average, while Track 9 (24 W, 500 mm s^{-1}) leads to the shortest grains; the remaining tracks produce major axes lengths in between. These results are consistent with the variations in the melt pool dimensions (cf. Table 4 and Fig. 4): Track 6 has the largest melt pool, while Track 9 is smallest. The measured depth and width of Track 5 would suggest that the obtained grain size should be in between Tracks 7 and 8. This trend is observed: until about 35 µm, the ECDF of Track 5 is in between those of Tracks 7 and 8, but for longer lengths the curves for Tracks 5 and 8 generally overlap. Given that the initial condition is identical for all five simulations, this behavior suggests that there is a particular set of grains that interacts with the boundaries of these three melt pools, and that we are observing changes in this comparatively small portion of the overall population.

In contrast, the ECDFs of the simulations are generally indistinguishable for the median and minor axes (Fig. 7b and c, respectively). For the median axis, we observe a slight increase in the average axis length compared to the input grain size. The average minor axis lengths slightly decrease, but visually the ECDFs are nearly identical to the input grain size distribution. On first examination, this may be a surprising outcome, but we perform the following thought experiment. Prior to melting and resolidification, all three principal axes should have identical length distributions that match the input grain size distribution, as the parent grains are nominally equiaxed. During the laser scan, grain boundaries located on the solid-liquid interface can nominally coarsen due to nonzero grain boundary mobility (Eqs. 23 and 24). However, the mobility of grain boundaries perpendicular to the solid-liquid interface quickly vanishes in the bulk material due to the sharp temperature gradient. The perpendicular boundaries in the bulk are essentially pinned, and any coarsening that does occur must produce curvature along the small mobile segments of the grain boundaries, which is energetically unfavorable. Large portions of the perpendicular grain boundaries inevitably melt, which creates only a narrow window of time for a grain on the melt pool surface to experience any measurable coarsening. Thus, the distributions of the median and minor axis lengths should reflect the average size of the intersecting plane, which is simply the grain size, plus some deviation due to a minimal amount of grain growth and the rotation of the interface that is forced by the changing melt pool location over time.

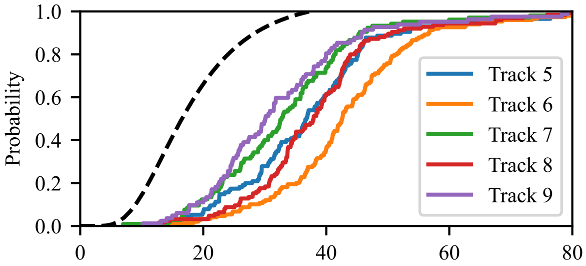

(a) Major Axis Length (μm)

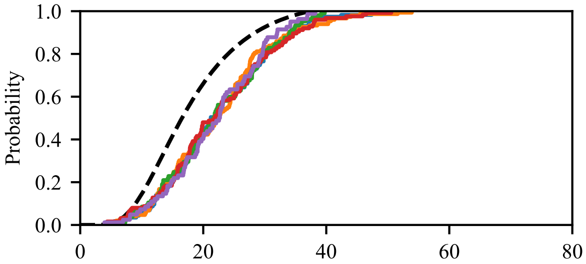

(b) Median Axis Length (μm)

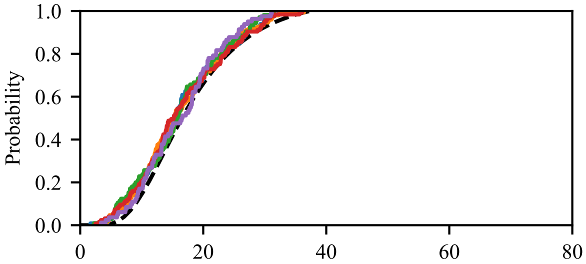

(c) Minor Axis Length (μm)

Figure 7: Empirical cumulative distribution functions of the (a) major, (b) median, and (c) minor axes lengths for the simulated tracks as indicated. Additionally, the CDF of the input grain size distribution is plotted for reference (dashed black line).

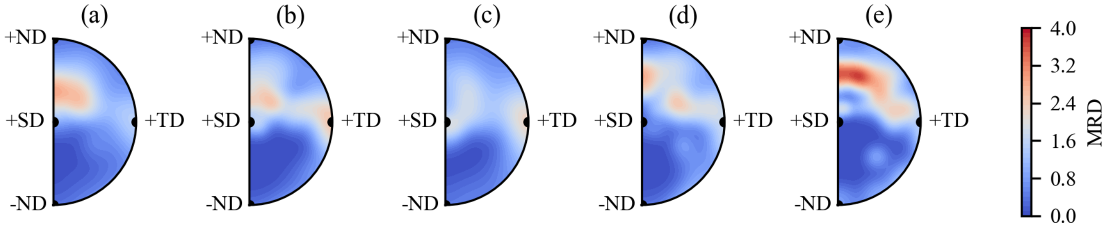

Figure 8: Orientation distributions of the major axis of the melted and resolidified grains from the simulations of (a) Track 5, (b) Track 7, (c) Track 9, (d), Track 8, and (e) Track 6. The ordering of the tracks is consistent with Fig. 5.

As a note, the minor axis distributions in Fig. 6 are different than the input grain size distribution, even if we do not filter out small features and considered all solidified grains on the top surface. This is expected with the 2D analysis, as there is a small probability that the minor axis lies exactly in the plane of the top surface. Prior to lasering, this is not a significant issue, as the grains are nominally equiaxed and the same stereological relationships that inform the grain size distribution are thus valid. This is no longer the case at the end of either the simulation or experiment, and thus we would likely need a very large dataset of grains that are properly bisected in order to observe this same trend. However, this emphasizes the need for 3D simulations and/or experimental characterization: the observed trend in the simulations indicate that the grains effectively elongate along a single axis, while the remaining directions are minimally affected. While beyond the scope of the present work, it may be worthwhile to investigate this trend across a wider range of grain size distributions (particularly with respect to the melt pool dimensions). If the insensitivity of the minor axis length distribution is a general behavior, then perhaps it could be exploited to "back calculate" the grain size distribution of a 3D experimental dataset obtained through serial sectioning or similar, eliminating the need to obtain reconstructions of the initial volume.

Next, we generate and plot orientation distribution functions (ODFs) for the major axis of each grain. Each principal axis has two equivalent directions; thus, we apply an inversion symmetry operation to the desired vector in $\mathbf{Q}_n$. Additionally, we assume that for a sufficiently long track the center of the laser track acts as a mirror plane, which allows the ODF to be represented on the half of the hemisphere that contains the positive scan direction (+SD), positive transverse direction (+TD), and both the positive and negative normal directions (±ND), where the normal is perpendicular to the planar surface. Each set of directions is converted from a discrete to a continuous representation by obtaining a kernel density estimator of the ODF using the scikit-learn Python package [87]. The ODFs of the major grain axes for each track are plotted in Fig. 8. In general, we observe that the highest probability regions for the major axis orientation are above the SD-TD plane and the lowest probability regions are below the SD-TD plane. The shape of the distribution indicates that the grains are aligned such that their major axes point towards the centerline of the laser scan path, which is consistent with the microstructures in Fig. 5 as well as previous studies [34]. However, the shape of the high probability region is different for each track due to changes in the geometry of their melt pools. Panels (a)–(c) contain the results for Tracks 5, 7, and 9 (increasing velocity). We observe that as velocity is increased, the highest probability shifts from an area between +ND and +SD towards an area between +SD and +TD, although the peak also becomes significantly more diffuse. This shift is likely due to the decreasing depth of the melt pool: fewer grains will remelt along the normal direction, therefore fewer grains may preferentially align in this direction. Likewise, if we consider Fig. 5(c)–(e) for Tracks 9, 8, and 6 (increasing power), we observe that the highest probability region gradually becomes a band that transitions between grains that are aligned in the SD-TD plane and grains aligned in the SD-ND plane. Tracks 6 and 8 are significantly larger than the other simulated conditions and more grains melt and resolidify; therefore, more grains will have an opportunity for their major axes to align. A critical consideration of Fig. 8 is that the major axis does not necessarily coincide with a $\langle 100 \rangle$ crystallographic direction due to the inclusion of twins and the nonzero solid-liquid mobility along other possible growth directions (cf. Fig. 5 and its discussion).

5. Conclusions

Here, we presented a combined experimental and simulation study of the microstructure that evolves during melting and resolidification of polycrystalline 316L stainless steel. The use of an *in situ* CW Laser-SEM device allowed for direct observation of the same locations in the microstructures before and after exposure with a minimal risk of damage to the specimen. This allowed for the collection of large datasets for comparison against a coupled phase-field and thermal multiphysics model of the melting and resolidification process.

We make the following conclusions of the present study:

1. The calibrated multiphysics model predicts melt pool widths and depths that are in good agreement with those measured from the experimental microstructures, which is critical to predicting the resulting microstructures.
2. As-printed microstructures predicted by the phase-field modeling framework reproduce many qualitative and quantitative aspects of the experimentally-observed microstructures. Qualitatively, we observe that the considered range of laser powers and scan velocities produces grains with varying degrees of curvature along their solidification length. These grains may preferentially align with the scanning direction of the laser, depending on the chosen power and velocity; grains with the largest melt pools are typically more normal to the scan direction than the smallest melt pools. Even for the lowest input energy density, a minimal amount of melting and resolidification is observed, despite the melt pool dimensions being comparable to the grain size.
3. The top surfaces of the simulated microstructures predict equivalent ellipses with similar major and minor axes, orientations, and aspect ratios as those obtained from the experiments. Empirical cumulative distribution functions of the simulated quantities either overlap with those from the experiment or agree within an estimated confidence interval. Combined with the melt pool dimensions predicted by the multiphysics framework, we conclude that the overall modeling framework is validated for predicting the microstructures observed with the novel CW Laser-SEM device [44, 45]. This device is capable of simulating a wide range of thermal process conditions that are characteristic of AM and other laser-based processing techniques, including at higher velocities and laser powers than are considered in the present study. The combination of the CW Laser-SEM device and the coupled modeling framework can thus be leveraged for further physical simulation of laser-based processing. While the present study neglects the addition of feedstock material, the characteristic epitaxial grain growth that occurs within a single track is well captured.
4. In three-dimensional analyses of the simulations, the major axis length is most affected by the change in melt pool conditions. The median axis length changes during processing, but both the median and minor axis length distributions appear to be relatively insensitive to changes in the scanning conditions.
5. Changes in the melt pool geometry produce variations in the major axis orientation of the resolidified grains. Strong preferential alignment of the major axis can occur for certain melt pool conditions. The presence of twins in the microstructure introduces additional crystallographic directions with preferential growth, but twinned portions of grains do not necessarily have different alignment with the axis of the laser scan. Thus, while the major axis of the overall grain is not necessarily aligned with the preferred directions of the parent or twin, the final microstructure is sensitive to the presence of twins in the preexisting microstructure.

Acknowledgements

The authors thank Dr. David Rowenhorst at the U.S. Naval Research Laboratory for helpful discussions on the inclusion of twins in the simulated microstructures.

AFC and PWV acknowledge support from the Office of Naval Research (ONR) under project number N00014-18-1-2782 P00002 and the National Institute for Standards and Technology (NIST) through the Center for Hierarchical Materials Design (CHiMaD) at Northwestern University under contract 70NANB19H005. JGSM and MVU are grateful to the European Research Council (ERC) for their support through the European Union's Horizon 2020 research and innovation program for project GAMMA (Grant agreement No. 946959). JGSM and MVU would also like to thank LMS for providing financial support to build the CW laser-SEM system. AS and GJW were supported by the U.S. DEVCOM Army Research Laboratory, award W911NF-21-2-02199.

This research was supported in part through the computational resources and staff contributions provided for the Quest high performance computing facility at Northwestern University, which is jointly supported by the Office of the Provost, the Office for Research, and Northwestern University Information Technology. Additional support was provided by Anvil at Purdue University through allocations MAT220009 and MAT220026 from the Advanced Cyberinfrastructure Coordination Ecosystem: Services & Support (ACCESS) program, which is supported by National Science Foundation grants #2138259, #2138286, #2138307, #2137603, and #2138296.

This research was performed while AFC was previously employed at Northwestern University. The conclusions and opinions are the authors' own and do not reflect the views of the United States Government, the U.S. Naval Research Laboratory, or the U.S. Army Research Laboratory.

References

[1] T. Mukherjee, J. W. Elmer, H. L. Wei, T. J. Lienert, W. Zhang, S. Kou, T. DebRoy, Control of grain structure, phases, and defects in additive manufacturing of high-performance metallic components, Prog. Mater. Sci. 138 (2023) 101153. `doi:10.1016/j.pmatsci.2023.101153`.

[2] S. Ghosh, J. Zollinger, M. Zaloznik, D. Banerjee, C. K. Newman, R. Arroyave, Modeling of hierarchical solidification microstructures in metal additive manufacturing: Challenges and opportunities, Addit. Manuf. 78 (2023) 103845. `doi:10.1016/j.addma.2023.103845`.

[3] T. Q. Phan, M. Strantza, M. R. Hill, T. H. Gnaupel-Herold, J. Heigel, C. R. D'Elia, A. T. DeWald, B. Clausen, D. C. Pagan, J. Y. Peter Ko, D. W. Brown, L. E. Levine, Elastic Residual Strain and Stress Measurements and Corresponding Part Deflections of 3D Additive Manufacturing Builds of IN625 AM-Bench Artifacts Using Neutron Diffraction, Synchrotron X-Ray Diffraction, and Contour Method, Integr. Mater. Manuf. Innov. 8 (3) (2019) 318–334. `doi:10.1007/s40192-019-00149-0`.

[4] J. C. Heigel, B. Lane, L. Levine, T. Phan, J. Whiting, In Situ Thermography of the Metal Bridge Structures Fabricated for the 2018 Additive Manufacturing Benchmark Test Series (AM-Bench 2018), J. Res. Natl. Inst. Stand. Technol. 125 (2020) 125005. `doi:10.6028/jres.125.005`.

[5] A. C. Chuang, J.-S. Park, P. A. Shade, E. J. Schwalbach, M. A. Groeber, W. D. Musinski, AFRL Additive Manufacturing Modeling Series: Challenge 1, Characterization of Residual Strain Distribution in Additively-Manufactured Metal Parts Using Energy-Dispersive Diffraction, Integr. Mater. Manuf. Innov. 10 (4) (2021) 525–541. `doi:10.1007/s40192-021-00233-4`.

[6] M. G. Chapman, M. N. Shah, S. P. Donegan, J. M. Scott, P. A. Shade, D. Menasche, M. D. Uchic, AFRL Additive Manufacturing Modeling Series: Challenge 4, 3D Reconstruction of an IN625 High-Energy Diffraction Microscopy Sample Using Multi-modal Serial Sectioning, Integr. Mater. Manuf. Innov. 10 (2) (2021) 129–141. `doi:10.1007/s40192-021-00212-9`.

[7] L. Levine, B. Lane, J. Heigel, K. Migler, M. Stoudt, T. Phan, R. Ricker, M. Strantza, M. Hill, F. Zhang, J. Seppala, E. Garboczi, E. Bain, D. Cole, A. Allen, J. Fox, C. Campbell, Outcomes and Conclusions from the 2018 AM-Bench Measurements, Challenge Problems, Modeling Submissions, and Conference, Integr. Mater. Manuf. Innov. 9 (1) (2020) 1–15. `doi:10.1007/s40192-019-00164-1`.

[8] J. Akram, P. Chalavadi, D. Pal, B. Stucker, Understanding grain evolution in additive manufacturing through modeling, Addit. Manuf. 21 (2018) 255–268. `doi:10.1016/j.addma.2018.03.021`.

[9] Th. Camus, D. Maisonnette, O. Baulin, O. Senninger, G. Guillemot, C. A. Gandin, Three-dimensional modeling of solidification grain structures generated by laser powder bed fusion, Materialia 30 (2023) 101804. `doi:10.1016/j.mtla.2023.101804`.

[10] A. R. A. Dezfoli, W.-S. Hwang, W.-C. Huang, T.-W. Tsai, Determination and controlling of grain structure of metals after laser incidence: Theoretical approach, Sci. Rep. 7 (1) (2017) 41527. `doi:10.1038/srep41527`.

[11] S. M. Elahi, R. Tavakoli, I. Romero, D. Tourret, Grain growth competition during melt pool solidification — Comparing phase-field and cellular automaton models, Comput. Mater. Sci. 216 (2023) 111882. `doi:10.1016/j.commatsci.2022.111882`.

[12] C. Herriott, X. Li, N. Kouraytem, V. Tari, W. Tan, B. Anglin, A. D. Rollett, A. D. Spear, A multi-scale, multi-physics modeling framework to predict spatial variation of properties in additive-manufactured metals, Modell. Simul. Mater. Sci. Eng. 27 (2) (2019) 025009. `doi:10.1088/1361-651X/aaf753`.

[13] K. L. Johnson, T. M. Rodgers, O. D. Underwood, J. D. Madison, K. R. Ford, S. R. Whetten, D. J. Dagel, J. E. Bishop, Simulation and experimental comparison of the thermo-mechanical history and 3D microstructure evolution of 304L stainless steel tubes manufactured using LENS, Comput. Mech. 61 (5) (2018) 559–574. `doi:10.1007/s00466-017-1516-y`.

[14] G. L. Knapp, J. Coleman, M. Rolchigo, M. Stoyanov, A. Plotkowski, Calibrating uncertain parameters in melt pool simulations of additive manufacturing, Comput. Mater. Sci. 218 (2023) 111904. `doi:10.1016/j.commatsci.2022.111904`.

[15] Y. Lian, S. Lin, W. Yan, W. K. Liu, G. J. Wagner, A parallelized three-dimensional cellular automaton model for grain growth during additive manufacturing, Comput. Mech. 61 (5) (2018) 543–558. `doi:10.1007/s00466-017-1535-8`.

[16] Y. Lian, Z. Gan, C. Yu, D. Kats, W. K. Liu, G. J. Wagner, A cellular automaton finite volume method for microstructure evolution during additive manufacturing, Mater. Des. 169 (2019) 107672. `doi:10.1016/j.matdes.2019.107672`.

[17] J. G. Pauza, W. A. Tayon, A. D. Rollett, Computer simulation of microstructure development in powder-bed additive manufacturing with crystallographic texture, Modell.d Simul. Mater. Sci. Eng. 29 (5) (2021) 055019. `doi:10.1088/1361-651X/ac03a6`.

[18] J. Pauza, A. Rollett, Simulation Study of Hatch Spacing and Layer Thickness Effects on Microstructure in Laser Powder Bed Fusion Additive Manufacturing using a Texture-Aware Solidification Potts Model, J. Mater. Eng. Perform. 30 (9) (2021) 7007–7018. `doi:10.1007/s11665-021-06110-7`.

[19] A. Rai, M. Markl, C. Körner, A coupled Cellular Automaton–Lattice Boltzmann model for grain structure simulation during additive manufacturing, Comput. Mater. Sci. 124 (2016) 37–48. `doi:10.1016/j.commatsci.2016.07.005`.

[20] T. M. Rodgers, J. A. Mitchell, V. Tikare, A Monte Carlo model for 3D grain evolution during welding, Modell. Simul. Mater. Sci. Eng. 25 (6) (2017) 064006. `doi:10.1088/1361-651X/aa7f20`.

[21] T. M. Rodgers, J. D. Madison, V. Tikare, Simulation of metal additive manufacturing microstructures using kinetic Monte Carlo, Comput. Mater. Sci. 135 (2017) 78–89. `doi:10.1016/j.commatsci.2017.03.053`.

[22] T. M. Rodgers, J. E. Bishop, J. D. Madison, Direct numerical simulation of mechanical response in synthetic additively manufactured microstructures, Modell. Simul. Mater. Sci. Eng. 26 (5) (2018) 055010. `doi:10.1088/1361-651X/aac616`.

[23] M. Rolchigo, J. Coleman, G. L. Knapp, A. Plotkowski, Grain structure and texture selection regimes in metal powder bed fusion, Addit. Manuf. 81 (2024) 104024. `doi:10.1016/j.addma.2024.104024`.

[24] R. Shi, S. A. Khairallah, T. T. Roehling, T. W. Heo, J. T. McKeown, M. J. Matthews, Microstructural control in metal laser powder bed fusion additive manufacturing using laser beam shaping strategy, Acta Mater. 184 (2020) 284–305. `doi:10.1016/j.actamat.2019.11.053`.

[25] B. C. Stump, A. Plotkowski, J. Nutaro, DECA: Discrete Event inspired Cellular Automata for grain structure prediction in additive manufacturing, Comput. Mater. Sci. 237 (2024) 112901. `doi:10.1016/j.commatsci.2024.112901`.

[26] K. Teferra, D. J. Rowenhorst, Optimizing the cellular automata finite element model for additive manufacturing to simulate large microstructures, Acta Mater. 213 (2021) 116930. `doi:10.1016/j.actamat.2021.116930`.

[27] C. Xue, N. Blanc, F. Soulié, C. Bordreuil, F. Deschaux-Beaume, G. Guillemot, M. Bellet, C.-A. Gandin, Structure and texture simulations in fusion welding processes – comparison with experimental data, Materialia 21 (2022) 101305. `doi:10.1016/j.mtla.2021.101305`.

[28] W. Yan, Y. Lian, C. Yu, O. L. Kafka, Z. Liu, W. K. Liu, G. J. Wagner, An integrated process–structure–property modeling framework for additive manufacturing, Comput. Methods Appl. Mech. Eng. 339 (2018) 184–204. `doi:10.1016/j.cma.2018.05.004`.

[29] O. Zinovieva, A. Zinoviev, V. Ploshikhin, Three-dimensional modeling of the microstructure evolution during metal additive manufacturing, Comput. Mater. Sci. 141 (2018) 207–220. `doi:10.1016/j.commatsci.2017.09.018`.

[30] C. A. Gandin, J. L. Desbiolles, M. Rappaz, Ph. Thevoz, A three-dimensional cellular automation-finite element model for the prediction of solidification grain structures, Metall. Mater. Trans. A 30 (12) (1999) 3153–3165. `doi:10.1007/s11661-999-0226-2`.

[31] T. Pinomaa, J. M. McKeown, J. M. Wiezorek, N. Provatas, A. Laukkanen, T. Suhonen, Phase field modeling of rapid resolidification of Al-Cu thin films, J. Cryst. Growth 532 (2020) 125418. `doi:10.1016/j.jcrysgro.2019.125418`.

[32] K. Karayagiz, L. Johnson, R. Seede, V. Attari, B. Zhang, X. Huang, S. Ghosh, T. Duong, I. Karaman, A. Elwany, R. Arróyave, Finite interface dissipation phase field modeling of Ni–Nb under additive manufacturing conditions, Acta Mater. 185 (2020) 320–339. `doi:10.1016/j.actamat.2019.11.057`.

[33] M. Yang, L. Wang, W. Yan, Phase-field modeling of grain evolutions in additive manufacturing from nucleation, growth, to coarsening, npj Comput. Mater. 7 (1) (2021) 56. `doi:10.1038/s41524-021-00524-6`.

[34] A. F. Chadwick, P. W. Voorhees, The development of grain structure during additive manufacturing, Acta Mater. 211 (2021) 116862. `doi:10.1016/j.actamat.2021.116862`.

[35] Y. Qin, Y. Bao, S. DeWitt, B. Radhakrishnan, G. Biros, Dendrite-resolved, full-melt-pool phase-field simulations to reveal non-steady-state effects and to test an approximate model, Comput. Mater. Sci. 207 (2022) 111262. `doi:10.1016/j.commatsci.2022.111262`.

[36] A. F. Chadwick, P. W. Voorhees, Recursive grain remapping scheme for phase-field models of additive manufacturing, Int. J. Numer. Meth. Eng. 123 (13) (2022) 3093–3110. `doi:10.1002/nme.6966`.

[37] A. F. Chadwick, P. W. Voorhees, The effects of melt pool geometry and scan strategy on microstructure development during additive manufacturing, IOP Conf. Ser. Mater. Sci. Eng. 1274 (1) (2023) 012010. `doi:10.1088/1757-899X/1274/1/012010`.

[38] T. Takaki, Y. Takahashi, S. Sakane, Multi-Phase-Field Framework for Epitaxial Grain Growth in Selective Laser Melting Additive Manufacturing with Multi-Track and Multi-Layer, Mater. Trans. 64 (6) (2023) 1150–1159. `doi:10.2320/matertrans.MT-ME2022014`.

[39] T. Keller, G. Lindwall, S. Ghosh, L. Ma, B. M. Lane, F. Zhang, U. R. Kattner, E. A. Lass, J. C. Heigel, Y. Idell, M. E. Williams, A. J. Allen, J. E. Guyer, L. E. Levine, Application of finite element, phase-field, and CALPHAD-based methods to additive manufacturing of Ni-based superalloys, Acta Mater. 139 (2017) 244–253. `doi:10.1016/j.actamat.2017.05.003`.

[40] S. M. Elahi, R. Tavakoli, A. K. Boukellal, T. Isensee, I. Romero, D. Tourret, Multiscale simulation of powder-bed fusion processing of metallic alloys, Comput. Mater. Sci. 209 (2022) 111383. `doi:10.1016/j.commatsci.2022.111383`.

[41] M. Lindroos, T. Pinomaa, K. Ammar, A. Laukkanen, N. Provatas, S. Forest, Dislocation density in cellular rapid solidification using phase field modeling and crystal plasticity, Int. J. Plast. 148 (2022) 103139. `doi:10.1016/j.ijplas.2021.103139`.

[42] P. W. Liu, Y. Z. Ji, Z. Wang, C. L. Qiu, A. A. Antonysamy, L. Q. Chen, X. Y. Cui, L. Chen, Investigation on evolution mechanisms of site-specific grain structures during metal additive manufacturing, J. Mater. Proc. Technol. 257 (2018) 191–202. `doi:10.1016/j.jmatprotec.2018.02.042`.

[43] S. A. Nabavizadeh, M. Eshraghi, S. D. Felicelli, Three-dimensional phase field modeling of columnar to equiaxed transition in directional solidification of Inconel 718 alloy, J. Cryst. Growth 549 (2020) 125879. `doi:10.1016/j.jcrysgro.2020.125879`.

[44] J. G. Santos Macías, K. Chen, A. Tanguy, M. Vallet, L. Cornet, V. Michel, M. V. Upadhyay, Micron-sized lasering improves mechanical behaviour of additively manufactured stainless steels, Under review (Oct. 2024).
URL `https://hal.science/hal-04530203`

[45] N. Mohanan, J. G. S. Macías, J. Bleyer, T. Helfer, M. V. Upadhyay, Intergranular stress and plastic strain formation during laser scanning of additively manufactured stainless steel: An experimentally-driven thermomechanical simulation study, Materialia 34 (2024) 102082. `doi:https://doi.org/10.1016/j.mtla.2024.102082`.

[46] A. Samaei, Z. Sang, J. A. Glerum, J.-E. Mogonye, G. J. Wagner, Multiphysics modeling of mixing and material transport in additive manufacturing with multicomponent powder beds, Addit. Manuf. 67 (2023) 103481. `doi:10.1016/j.addma.2023.103481`.

[47] A. Samaei, J. P. Leonor, Z. Gan, Z. Sang, X. Xie, B. J. Simonds, W. K. Liu, G. J. Wagner, Benchmark study of melt pool and keyhole dynamics, laser absorptance, and porosity in additive manufacturing of ti-6al-4v, Prog. Addit. Manuf. (2024) 1–25`doi:10.1007/s40964-024-00637-6`.

[48] J.-H. Cho, S.-J. Na, Implementation of real-time multiple reflection and Fresnel absorption of laser beam in keyhole, J. Phys. D Appl. Phys. 39 (24) (2006) 5372–5378. `doi:10.1088/0022-3727/39/24/039`.

[49] B. Liu, G. Fang, L. Lei, W. Liu, A new ray tracing heat source model for mesoscale CFD simulation of selective laser melting (SLM), Appl. Math. Model. 79 (2020) 506–520. `doi:10.1016/j.apm.2019.10.049`.

[50] M. Bayat, A. Thanki, S. Mohanty, A. Witvrouw, S. Yang, J. Thorborg, N. S. Tiedje, J. H. Hattel, Keyhole-induced porosities in Laser-based Powder Bed Fusion (L-PBF) of Ti6Al4V: High-fidelity modelling and experimental validation, Addit. Manuf. 30 (2019) 100835. `doi:10.1016/j.addma.2019.100835`.

[51] R. Ducharme, K. Williams, P. Kapadia, J. Dowden, B. Steen, M. Glowacki, The laser welding of thin metal sheets: An integrated keyhole and weld pool model with supporting experiments, Journal of Physics D: Applied Physics 27 (8) (1994) 1619. `doi:10.1088/0022-3727/27/8/006`.

[52] P. Martin, G. Guillemot, C. A. Hareland, P. W. Voorhees, C.-A. Gandin, Kinetic effects during the plane-front and dendritic solidification of multicomponent alloys, Acta Materialia 263 (2024) 119473. `doi:10.1016/j.actamat.2023.119473`.

[53] S. David, J. Vitek, R. Reed, T. Hebble, Effect of rapid solidification on stainless steel weld metal microstructures and its implications on the Schaeffler diagram, Tech. Rep. ORNL/TM-10487, 5957599, Oak Ridge National Laboratory, Oak Ridge, Tennessee (Sep. 1987). `doi:10.2172/5957599`.

[54] S. Fukumoto, W. Kurz, Prediction of the δ to γ Transition in Austenitic Stainless Steels during Laser Treatment., ISIJ International 38 (1) (1998) 71–77. `doi:10.2355/isijinternational.38.71`.

[55] S. Fukumoto, W. Kurz, Solidification Phase and Microstructure Selection Maps for Fe-Cr-Ni Alloys., ISIJ International 39 (12) (1999) 1270–1279. `doi:10.2355/isijinternational.39.1270`.

[56] S. Ghosh, A. Karma, M. Plapp, S. Akamatsu, S. Bottin-Rousseau, G. Faivre, Influence of morphological instability on grain boundary trajectory during directional solidification, Acta Materialia 175 (2019) 214–221. `doi:10.1016/j.actamat.2019.04.054`.

[57] N. Moelans, A quantitative and thermodynamically consistent phase-field interpolation function for multi-phase systems, Acta Mater. 59 (3) (2011) 1077–1086. `doi:10.1016/j.actamat.2010.10.038`.

[58] G. I. Tóth, T. Pusztai, L. Gránásy, Consistent multiphase-field theory for interface driven multidomain dynamics, Phys. Rev. B 92 (18) (2015) 184105. `doi:10.1103/PhysRevB.92.184105`.

[59] N. Moelans, B. Blanpain, P. Wollants, Quantitative analysis of grain boundary properties in a generalized phase field model for grain growth in anisotropic systems, Phys. Rev. B 78 (2) (2008) 024113–024113. `doi:10.1103/PhysRevB.78.024113`.

[60] I. Flow Science, FLOW-3D, Version 2023R1, Santa Fe, NM (2023).
URL `https://www.flow3d.com/`

[61] C. S. Kim, Thermophysical Properties of Stainless Steels, Tech. Rep. ANL-75-55, Argonne National Laboratory, Argonne, IL (1975).

[62] T. L. Bergman, F. P. Incropera (Eds.), Fundamentals of Heat and Mass Transfer, 7th Edition, Wiley, Hoboken, NJ, 2011.

[63] K. C. Mills, Recommended Values of Thermophysical Properties for Selected Commercial Alloys, Woodhead, Cambridge, 2002.

[64] P. Pichler, B. J. Simonds, J. W. Sowards, G. Pottlacher, Measurements of thermophysical properties of solid and liquid NIST SRM 316L stainless steel, Journal of Materials Science 55 (9) (2020) 4081–4093. `doi:10.1007/s10853-019-04261-6`.

[65] H. Fukuyama, H. Higashi, H. Yamano, Effect of B4C addition on the solidus and liquidus temperatures, density and surface tension of type 316 austenitic stainless steel in the liquid state, Journal of Nuclear Materials 554 (2021) 153100. `doi:10.1016/j.jnucmat.2021.153100`.

[66] K. Ueno, Y. Shibuta, Solid-liquid Interfacial Energy for Fe–Cr Alloy under Temperature Gradient from Molecular Dynamics Simulation, ISIJ Int. 60 (11) (2020) 2301–2305. `doi:10.2355/isijinternational.ISIJINT-2019-769`.

[67] D. Y. Sun, M. Asta, J. J. Hoyt, Crystal-melt interfacial free energies and mobilities in fcc and bcc Fe, Phys. Rev. B 69 (17) (2004) 174103. `doi:10.1103/PhysRevB.69.174103`.

[68] R. A. Varin, Grain boundary diffusion and free energy during the recrystallization of type 316 stainless steel, Mater. Sci. Eng. 66 (1) (1984) 97–105. `doi:10.1016/0025-5416(84)90144-7`.

[69] B. Kashyap, K. Tangri, Grain growth behaviour of type 316L stainless steel, Mater. Sci. Eng. A 149 (2) (1992) L13–L16. `doi:10.1016/0921-5093(92)90392-E`.

[70] R. Saye, High-order methods for computing distances to implicitly defined surfaces, Comm. Appl. Math. Comput. Sci. 9 (1) (2014) 107–141. `doi:10.2140/camcos.2014.9.107`.

[71] K. Glasner, Nonlinear preconditioning for diffuse interfaces, J. Comput. Phys. 174 (2) (2001) 695–711. `doi:10.1006/jcph.2001.6933`.

[72] A. Kumar, Isotropic finite-differences, J. Comput. Phys. 201 (1) (2004) 109–118. `doi:10.1016/j.jcp.2004.05.005`.

[73] A. C. Hindmarsh, P. N. Brown, K. E. Grant, S. L. Lee, R. Serban, D. E. Shumaker, C. S. Woodward, SUNDIALS: Suite of nonlinear and differential/algebraic equation solvers, ACM Trans. Math. Softw. 31 (3) (2005) 363–396. `doi:10.1145/1089014.1089020`.

[74] S. Vedantam, B. S. V. Patnaik, Efficient numerical algorithm for multiphase field simulations, Phys. Rev. E 73 (1) (2006) 016703. `doi:10.1103/PhysRevE.73.016703`.

[75] Y. Suwa, Y. Saito, H. Onodera, Phase field simulation of grain growth in three dimensional system containing finely dispersed second-phase particles, Scripta Mater. 55 (4) (2006) 407–410. `doi:10.1016/j.scriptamat.2006.03.034`.

[76] F. Bachmann, R. Hielscher, H. Schaeben, Grain detection from 2d and 3d EBSD data—Specification of the MTEX algorithm, Ultramicroscopy 111 (12) (2011) 1720–1733. `doi:10.1016/j.ultramic.2011.08.002`.

[77] E. E. Underwood, Quantitative Stereology for Microstructural Analysis, in: J. L. McCall, W. M. Mueller (Eds.), Microstructural Analysis: Tools and Techniques, Springer US, Boston, MA, 1973, pp. 35–66. `doi:10.1007/978-1-4615-8693-7\_3`.

[78] M. A. Groeber, M. A. Jackson, DREAM.3D: A digital representation environment for the analysis of microstructure in 3D, Integr. Mater. Manuf. Innov. 3 (1) (2014) 5–5. `doi:10.1186/2193-9772-3-5`.

[79] A. J. Birnbaum, J. C. Steuben, E. J. Barrick, A. P. Iliopoulos, J. G. Michopoulos, Intrinsic strain aging, $\Sigma 3$ boundaries, and origins of cellular substructure in additively manufactured 316L, Addit. Manuf. 29 (2019) 100784. `doi:10.1016/j.addma.2019.100784`.

[80] Y. Wang, C. Yu, L. Xing, K. Li, J. Chen, W. Liu, J. Ma, Z. Shen, Grain structure and texture of the SLM single track, J. Mater. Proc. Technol. 281 (2020) 116591. `doi:10.1016/j.jmatprotec.2020.116591`.

[81] Y. Balit, E. Charkaluk, A. Constantinescu, Digital image correlation for microstructural analysis of deformation pattern in additively manufactured 316L thin walls, Addit. Manuf. 31 (2020) 100862. `doi:10.1016/j.addma.2019.100862`.

[82] D. G. Brandon, The structure of high-angle grain boundaries, Acta Metall. 14 (11) (1966) 1479–1484. `doi:10.1016/0001-6160(66)90168-4`.

[83] S. van der Walt, J. L. Schönberger, J. Nunez-Iglesias, F. Boulogne, J. D. Warner, N. Yager, E. Gouillart, T. Yu, Scikit-image: Image processing in Python, PeerJ 2 (2014) e453. `doi:10.7717/peerj.453`.

[84] I. M. McKenna, M. P. Gururajan, P. W. Voorhees, Phase field modeling of grain growth: Effect of boundary thickness, triple junctions, misorientation, and anisotropy, J. Mater. Sci. 44 (9) (2009) 2206–2217. `doi:10.1007/s10853-008-3196-7`.

[85] M. Naaman, On the tight constant in the multivariate Dvoretzky–Kiefer–Wolfowitz inequality, Stat. Probabil. Lett. 173 (2021) 109088. `doi:10.1016/j.spl.2021.109088`.

[86] J. P. MacSleyne, J. P. Simmons, M. De Graef, On the use of moment invariants for the automated analysis of 3D particle shapes, Model. Simul. Mater. Sci. Eng. 16 (4) (2008) 045008. `doi:10.1088/0965-0393/16/4/045008`.

[87] F. Pedregosa, G. Varoquaux, A. Gramfort, V. Michel, B. Thirion, O. Grisel, M. Blondel, P. Prettenhofer, R. Weiss, V. Dubourg, J. Vanderplas, A. Passos, D. Cournapeau, M. Brucher, M. Perrot, E. Duchesnay, Scikit-learn: Machine learning in Python, J. Mach. Learn. Res. 12 (2011) 2825–2830.